

Pixel-wise Attentional Gating for Scene Parsing

Shu Kong, Charless Fowlkes
Department of Computer Science,
University of California, Irvine, CA 92697, USA
{skong2, fowlkes}@ics.uci.edu

[\[Project Page\]](#) [\[Github\]](#), [\[Slides\]](#)

Abstract

To achieve dynamic inference in pixel labeling tasks, we propose Pixel-wise Attentional Gating (PAG), which learns to selectively process a subset of spatial locations at each layer of a deep convolutional network. PAG is a generic, architecture-independent, problem-agnostic mechanism that can be readily “plugged in” to an existing model with fine-tuning. We utilize PAG in two ways: 1) learning spatially varying pooling fields that improve model performance without the extra computation cost associated with multi-scale pooling, and 2) learning a dynamic computation policy for each pixel to decrease total computation (FLOPs) while maintaining accuracy.

We extensively evaluate PAG on a variety of per-pixel labeling tasks, including semantic segmentation, boundary detection, monocular depth and surface normal estimation. We demonstrate that PAG allows competitive or state-of-the-art performance on these tasks. Our experiments show that PAG learns dynamic spatial allocation of computation over the input image which provides better performance trade-offs compared to related approaches (e.g., truncating deep models or dynamically skipping whole layers). Generally, we observe PAG can reduce computation by 10% without noticeable loss in accuracy and performance degrades gracefully when imposing stronger computational constraints.

1. Introduction

The development of deep convolutional neural networks (CNN) has allowed remarkable progress in wide range of image pixel-labeling tasks such as boundary detection [41, 56, 29], semantic segmentation [31, 32, 6], monocular depth estimation [32, 36, 35, 38, 13], and surface normal estimation [53, 4, 12]. Architectures that enable training of increasingly deeper networks have resulted in cor-

responding improvements in prediction accuracy [49, 22]. However, with great depth comes great computational burden. This hinders deployment of such deep models in edge and mobile computing applications which have significant power/memory constraints.

To make deep models more practically applicable, a flurry of recent work has focused on reducing these storage and computational costs [21, 42, 26, 40, 5, 30]. Static of-line techniques like network distillation [23], pruning [42], and model compression [5] take a trained network as input and synthesize a new network that approximates the same functionality with reduced memory footprint and test-time execution cost. Our approach is inspired by a complementary family of techniques that learn to vary the network computation depth adaptively, depending on the input data [51, 55, 54, 15].

In this paper, we study the problem of achieving dynamic inference for per-pixel labeling tasks with a deep CNN model under limited computational budget. For image classification, dynamic allocation of computational “attention” can be interpreted as expending more computation on ambiguous images (e.g., [51, 55, 54]) or limiting processing to informative image regions [15]. However, understanding the role of dynamic computation in pixel labeling tasks has not been explored. Pixel-level labeling requires analyzing fine-grained image details and making predictions at every spatial location, so it is not obvious that dynamically allocating computation to different image regions is useful. Unlike classification, labeling locally uninformative regions would seem to demand more computation rather than less (e.g., to incorporate long-range context).

To explore these questions, we introduce a *Pixel-wise Attentional Gating (PAG)* unit that selects a sparse subset of spatial locations to process based on the input feature map. We utilize the Gumbel sampling trick [19, 28, 39] to allow differentiable, end-to-end latent training of PAG units inserted across multiple computational blocks of a given task-specific architecture. We exploit this generic PAG unit in

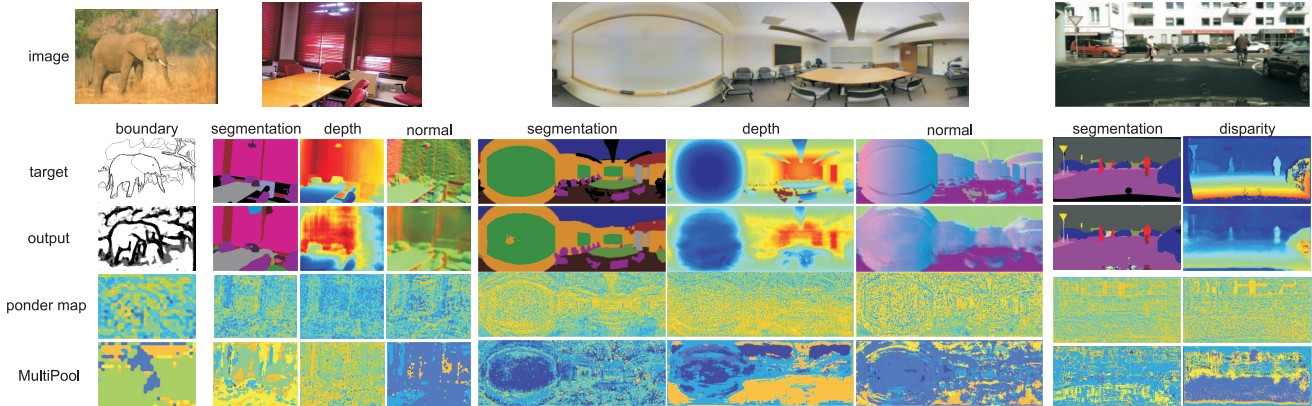


Figure 1: Pixel-wise Attentional Gating units (PAG) achieve dynamic inference by learning a dynamic computation path for each pixel under limited computation budget. The “ponder maps” shown in the last row provide a visualization of the amount of computation allocated to each location (generated by accumulating binary masks from PAG units across all layers); whereas the “MultiPool” adaptively chooses the proper pooling size for each pixel to aggregate information for inference. We apply PAG to a variety of per-pixel labeling tasks (boundary detection, semantic segmentation, monocular geometry) and evaluate over diverse image datasets (indoor/outdoor scenes, narrow/wide field-of-view).

two ways: bypassing sequential (residual) processing layers and dynamically selecting between multiple parallel network branches.

Dynamic computation depth: Inserting PAG at multiple layers of a Residual Network enables learning a dynamic, feed-forward computation path for each pixel that is conditional on the input image (see the second last row in Fig. 1). We introduce a sparsity hyperparameter that provides control over the average total and per-layer computation. For a fixed computational budget, we show this dynamic, per-pixel gating outperforms architectures that meet the budget by either using a smaller number of fixed layers or learning to dynamically bypass whole layers (Section 3.3).

Dynamic spatial pooling: We exploit PAG to dynamically select the extent of pooling regions at each spatial image location (see the last row in Fig. 1). Previous work has demonstrated the benefits of averaging features from multiple pooling scales using either learned weights [6], or spatially varying weights based on attention [7] or scene depth [32]. However, such multi-scale pooling requires substantially more computation. We show the proposed PAG unit can learn to select appropriate spatially-varying pooling, outperforming the recent work of [32] without the computational burden of multiple parallel branches (Section 3.4).

We carry out an extensive evaluation of pixel-wise attentional gating over diverse datasets for a variety of per-pixel labeling tasks including boundary detection, semantic segmentation, monocular depth estimation and surface normal estimation (see Fig. 1). We demonstrate that PAG helps deliver state-of-the-art performance on these tasks by dynamically allocating computation. In general, we observe that the introduction of PAG units can reduce total computa-

tion by 10% without noticeable drop in accuracy and shows graceful degradation in performance even with substantial budget constraints (e.g., a 30% budget cut).

To summarize our primary contribution: (1) we introduce a pixel-wise attentional gating unit which is problem-agnostic, architecture-independent and provides a simple method to allow user-specified control computational parsimony with standard training techniques; (2) we investigate the role of dynamic computation in pixel-labeling tasks and demonstrate improved prediction performance while maintaining or reducing overall compute cost.

2. Related Work

Deep CNN models with residual or “skip” connections have yielded substantial performance improvements with increased depth [22, 24], but also introduced redundant parameters and computation [21, 42]. In interpreting the success of residual networks (ResNet) [22], it has been suggested that ResNet can be seen as an ensemble of many small networks [52], each defined by a path through the network topology. This is supported by the observation that ResNet still performs well even when some layers are removed after training [25, 15]. This indicates it may be possible to reduce test-time computation by dynamically choosing only a subset of these paths to evaluate [51, 55, 54, 15].

This can be achieved by learning a halting policy that stops computation after evaluation of a particular layer [15], or a more flexible routing policy trained through reinforcement learning [55, 54]. Our method is most closely related to [51], which utilizes the “Gumbel sampling trick” [19, 28, 39] to learn binary gating that determines whether each layer is computed. The Gumbel sampling technique allows

one to perform gradient descent on models that include a discrete argmax operation without resorting to approximation by softmax or reinforcement learning techniques.

The PerforatedCNN [16] demonstrated that convolution operations could be accelerated by learning static masks that skip computation at a subset of spatial positions. This was used in [15] to achieve spatially varying dynamic depth. Our approach is simpler (it uses a simple sparsity regularization to directly control amount per-pixel or per-layer computation rather than ponder cost) and more flexible (allowing more flexible routing policies than early halting¹).

Finally, our use of dynamic computation to choose between branches is related to [32], which improves semantic segmentation by fusing features from multiple branches with various pooling sizes using a spatially varying weighted average. Unlike [6, 7, 32] which require computing the outputs of parallel pooling branches, our PAG-based learns to select a pooling size for each spatial location and only computes the necessary pooled features. This is similar in spirit to the work of [46], which demonstrated that sparsely-gated mixture-of-experts can dramatically increase model capacity using multi-branch configuration with only minor losses in computational efficiency.

3. Pixel-wise Attentional Gating

We first describe our design of Pixel-wise Attentional Gating (PAG) unit and its relation to the ResNet architecture [22]. Then, we elaborate how we exploit the Gumbel sampling technique to learning PAG differentiable even when generating binary masks. Finally we describe how the PAG unit can be used to perform dynamic inference by (1) selecting the subset of layers in the computational path for each spatial location, and (2) selecting the correct pooling size at each spatial location.

3.1. Plug-in PAG inside a Residual Block

Consider a block that computes output \mathbf{O} using a residual update $\mathbf{Z} = \mathcal{F}(\mathbf{I})$ to some input \mathbf{I} . To reduce computation, one can learn a gating function $\mathcal{G}(\mathbf{I})$ that selects a subset of spatial locations (pixels) to process conditional on the input. We represent the output of \mathcal{G} as a binary spatial mask \mathbf{G} which is replicated along feature channel dimension as needed to match dimension of \mathbf{O} and \mathbf{I} . The spatially gated residual update can be written as:

$$\begin{aligned} \mathbf{G} &= \mathcal{G}(\mathbf{I}) \\ \mathbf{O} &= \bar{\mathbf{G}} \odot \mathbf{I} + \mathbf{G} \odot (\mathcal{F}_{\mathbf{G}}(\mathbf{I}) + \mathbf{I}) \\ &= \mathbf{I} + \mathbf{G} \odot \mathcal{F}_{\mathbf{G}}(\mathbf{I}) \end{aligned} \quad (1)$$

where \odot is element-wise product, $\bar{\mathbf{G}} = 1 - \mathbf{G}$, and the notation $\mathcal{F}_{\mathbf{G}}$ indicates that we only evaluate \mathcal{F} at the locations

¹Results in [55, 54] suggest general routing offers better performance than truncating computation at a particular depth.

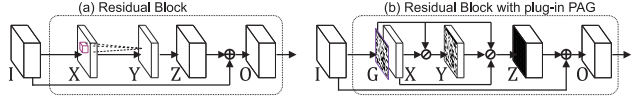


Figure 2: (a) A standard residual block. (b) Pixel-wise Attentional Gating unit (PAG) integrated into a residual block. Boxes/arrows denote activations/computations. \mathbf{G} is a sparse, binary map that modulates what processing applied to each spatial location. “ \odot ” means the perforated convolution [16], which assembles only active pixels for computation.

specified by \mathbf{G} . An alternative to spatially varying computation is for the gating function to predict a single binary value that determines whether or not the residual is calculated at this layer [51] in which case $\mathcal{F}_{\mathbf{G}}$ is only computed if $\mathbf{G} = 1$.

Both pixel-wise and layer-wise gating have the intrinsic limitation that the gating function \mathcal{G} must be evaluated prior to \mathcal{F} , inducing computational delays. To overcome this limitation we integrate the gating function more carefully within the ResNet block. We demonstrate ours in the equations below comparing a standard residual block (left) and the one with PAG (right), respectively with corresponding illustrations in Fig. 2:

$$\begin{aligned} \mathbf{X} &= \mathcal{F}^1(\mathbf{I}) & \mathbf{X} &= \mathcal{F}^1(\mathbf{I}), \quad \mathbf{G} = \mathcal{G}(\mathbf{I}) \\ \mathbf{Y} &= \mathcal{F}^2(\mathbf{X}) & \mathbf{Y} &= \mathcal{F}^2_{\mathbf{G}}(\mathbf{X}) \\ \mathbf{Z} &= \mathcal{F}^3(\mathbf{Y}) & \mathbf{Z} &= \mathcal{F}^3_{\mathbf{G}}(\bar{\mathbf{G}} \odot \mathbf{X} + \mathbf{G} \odot \mathbf{Y}) \\ \mathbf{O} &= \mathbf{I} + \mathbf{Z} & \mathbf{O} &= \mathbf{I} + \mathbf{Z} \end{aligned} \quad (2)$$

The transformation functions \mathcal{F} ’s consist of convolution, batch normalization [27] and ReLU [43] layers. As seen from the right set of equations, our design advocates computing the gating mask on the input \mathbf{I} to the current building block in parallel with $\mathbf{X} = \mathcal{F}_{\mathbf{X}}(\mathbf{I})$. ResNet adopts bottleneck structure so the first transformation \mathcal{F}^1 performs dimensionality reduction with a set of 1×1 kernels, \mathcal{F}^2 utilizes 3×3 kernels, and \mathcal{F}^3 is another transform with 1×1 kernels that restores dimensionality. As a result, the most costly computation is in the second transformation \mathcal{F}^2 which is mitigated by gating the computation. We show in our ablation study (Section 5.2) that for per-pixel labeling tasks, this design outperforms layer-wise gating.

3.2. Learning Discrete Attention Maps

The key to the proposed PAG is the gating function \mathcal{G} that produces a discrete (binary) mask which allows for reduced computation. However, producing the binary mask using hard thresholding is non-differentiable, and thus cannot be simply incorporated in CNN where gradient descent is used for training. To bridge the gap, we exploit the Gumbel-Max trick [19] and its recent continuous relaxation [39, 28].

A random variable m follows a Gumbel distribution if $m \equiv -\log(-\log(u))$, where u is a sample from the uniform distribution $u \sim \mathcal{U}[0, 1]$. Let g be a discrete ran-

dom variable with probabilities $P(g = k) \propto a_k$, and let $\{m_k\}_{k=1,\dots,K}$ be a sequence of i.i.d. Gumbel random variables. Then we can sample from the discrete variable with:

$$g = \operatorname{argmax}_{k=1,\dots,K} (\log \alpha_k + m_k) \quad (3)$$

The drawback of this approach is that the argmax operation is not continuous when mapping the Gumbel samples to the realizations of discrete distribution. To address this issue, a continuous relaxation the Gumbel Sampling Trick, proposed in [39, 28], replaces the argmax operation with a softmax. Using a one-hot vector $\mathbf{g} = [g_1, \dots, g_K]$ to encode g , a sample from the Gumbel softmax relaxation can be expressed by the vector:

$$\mathbf{g} = \operatorname{softmax}((\log(\boldsymbol{\alpha}) + \mathbf{m})/\tau) \quad (4)$$

where $\boldsymbol{\alpha} = [\alpha_1, \dots, \alpha_K]$, $\mathbf{m} = [m_1, \dots, m_K]$, and τ is the ‘‘temperature’’ parameter. In the limit as $\tau \rightarrow 0$, the softmax function approaches the argmax function and Eq. (4) becomes equivalent to the discrete sampler. Since the softmax function is differentiable and \mathbf{m} contains i.i.d Gumbel random variables which are independent to input activation $\boldsymbol{\alpha}$, we can easily propagate gradients to the probability vector $\boldsymbol{\alpha}$, which is treated as the gating mask for a single pixel in the per-pixel labeling tasks.

As suggested in [51], we employ the straight-through version [39] of Eq. (4) during training. In particular, for the forward pass, we use discrete samples from Eq. (3), but during the backwards pass, we compute the gradient of the softmax relaxation in Eq. (4). Based on our empirical observation as well as that reported in [39], such greedy straight-through estimator performs slightly better than strictly following Eq. (4), even though there is a mismatch between forward and backward pass. In our work, we initialize $\tau = 1$ and decrease it to 0.1 gradually during training. We find this works even better than training with a constant small τ .

3.3. Dynamic Per-Pixel Computation Routing

By stacking multiple PAG residual blocks, we can construct a model in which the subset of layers used to compute an output varies for each spatial location based the collection of binary masks. We allow the user to specify the computational budget in terms of a target sparsity ρ . For a binary mask $\mathbf{G} \in \{0, 1\}^{H \times W}$, we compute the empirical sparsity $g = \frac{1}{H \times W} \sum_{h,w} \mathbf{G}_{h,w}$ (smaller values indicate sparser computation) and measure how well it matches the target ρ using the KL divergence:

$$KL(\rho||g) \equiv \rho \log\left(\frac{\rho}{g}\right) + (1 - \rho) \log\left(\frac{1 - \rho}{1 - g}\right) \quad (5)$$

To train the model, we jointly minimize the sum of a task-specific loss ℓ_{task} and the per-layer sparsity loss

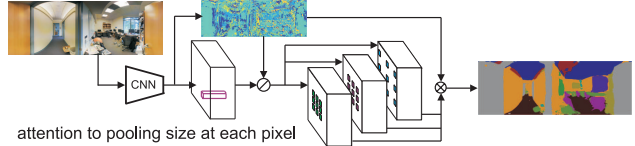


Figure 3: PAG-based MultiPool module learns to select the pooling size for each spatial location so that contextual information can be better aggregated. This can be implemented efficiently using perforated convolution [16], denoted by \odot , which assembles only active pixels for computation in each pooling branch and thus avoids computing all pooled versions.

summed over all layers of interest:

$$\ell = \ell_{task} + \lambda \sum_{l=1}^L KL(\rho||g_l) \quad (6)$$

where l indexes one of L layers which have PAG inserted for dynamic computation and λ controls the weight for the constraints. In our experiments we set $\lambda = 10^{-4}$ but found performance is stable over a wide range of penalties ($\lambda \in [10^{-5}, 10^{-2}]$). To visualize the spatial distribution of computation, we accumulate the binary gating masks from all to produce a ‘‘ponder map’’. This reveals that trained models do not allocate computation uniformly, but instead responds to image content (*e.g.* focusing computation on boundaries between objects where semantic labels, depths or surface normals undergo sharp changes).

An alternative to per-layer sparsity is to compute the total sparsity $g = \frac{1}{L} \sum_{l=1}^L g_l$ and penalize g with $KL(\rho||g)$. However, training in this way does not effectively learn dynamic computational paths and results in trivial, non-dynamic solutions, *e.g.* completely skipping a subset of layers and always using the remaining ones. Similar phenomenon is reported in [51]. In training models we typically start from a pre-trained model and insert sparsity constraints progressively. We found this incremental construction produces better diversity in the PAG computation paths. We also observe that when targeting reduced computation budget, fine-tuning a model which has already been trained with larger ρ consistently brings better performance than fine-tuning a pre-trained model directly with a small ρ .

3.4. Dynamic Spatial Pooling

In pixel-labeling tasks, the ideal spatial support for analyzing a pixel can vary over the visual field in order to simultaneously maintain fine-grained details and capture context. This suggests an adaptive pooling mechanism at pixel level, or multi-scale pooling module (*MultiPool*) that chooses the appropriate pooling size for each pixel (see *e.g.*, [32]). Given a collection of P pooled feature maps $\{\mathbf{M}_i\}_{i=1,\dots,P}$ which are computed in convolution with different dilate rates (Fig. 3), we can generate a MultiPool feature map $\mathbf{O} = \sum_i \mathbf{W}_i \odot \mathbf{M}_i$, where $\{\mathbf{W}_i\}_{i=1,\dots,P}$ are spatial selection masks, and \odot indicates element-wise product

between \mathbf{W}_i and each channel of \mathbf{M}_i . We utilize the PAG to generate binary weight \mathbf{W}_i that selects the “correct” pooling region at each spatial location by applying Eq. (4). This MultiPool module, illustrated in Fig. 3, can be inserted in place of regular pooling with little computational overhead and learned in a latent manner using the task-specific loss (no additional sparsity loss).

We implement pooling using a set of 3×3 -kernels applied at a set of user-specified dilation rates ($[0, 1, 2, 4, 6, 8, 10]$) [57]. A dilation rate of 0 means the input feature is simply copied into the output feature map. In our experiments, we observe that only a small portion of pixels are exactly copied for the final representation without being fed into any multi-pooling branches. Note that in Fig. 3, a multiplicative gating operation is shown for clarity, but an efficient implementation would utilize masking to directly select pixels in a matrix multiplication implementation of the convolutional layers in GPU or FPGA kernel [8, 45]. Our MultiPool module is thus distinct from [32] which use weighted averages over all intermediate feature activations from all branches for the final feature representation. Our approach selects a single pooling size for each pixel and hence does not require overhead of computing all branches.

4. Implementation and Training

While our PAG unit is agnostic to network architectures, in all our experiments we utilize ResNet [22] pre-trained on ImageNet [11] as the base model. We following [6, 32] and increase the output resolution of ResNet by removing the top global 7×7 pooling layer and the last two 2×2 pooling layers, replacing them with atrous convolution with dilation rate 2 and 4, respectively, to maintain a spatial sampling rate. Such a modification thus outputs predictions at $1/8$ the input resolution. Rather than up-sampling the output (or downsampling the ground-truth) $8 \times$ for benchmarking [6, 32], we find it better to apply a deconvolution layer followed by two or more convolutional layers before the final output.

We augment the training sets with random left-right flips and crops with 20-pixel margin and of size divisible by 8. When training the model, we fix the batch normalization, using the same constant global moments in both training and testing. This modification does not impact the performance and allows a batch size of one during training (a single input image per batch). We use the “poly” learning rate policy [6] with a base learning rate of 0.0002 scaled as a function of iteration by $(1 - \frac{iter}{maxiter})^{0.9}$. We adopt a stage-wise training strategy over all tasks, *i.e.* training a base model, adding PAG-based MultiPool, inserting PAG for dynamic computation progressively, and finally decreasing ρ to achieve target computational budget. Since our goal is to explore computational parsimony in per-pixel labeling tasks, we implement our models without “bells and whis-

les”, *e.g.* no utilization of ensembles, no CRF as post-processing, and no external training data. We implement our approach using the toolbox MatConvNet [50], and train using SGD on a single Titan X GPU².

4.1. Per-Pixel Labeling Vision Tasks

Boundary Detection We train a base model using (binary) logistic loss. Following [56, 41, 31], we include four prediction branches at macro residual blocks (denoted by Res 2, 3, 4, 5) and a fusion branch for training. To handle class imbalance, we utilize a weighted loss accumulated over the prediction losses given by:

$$\ell_{boundary} = - \sum_{b \in \mathcal{B}} \sum_{j \in \mathcal{Y}} \beta_{y_j} \log(P(y_j | \theta_b)) \quad (7)$$

where b indexes the branches, $\beta_+ = |Y_-| / |Y_- \cup Y_+|$, $\beta_- = 1 - \beta_+$; Y_+ and Y_- denote the set of boundary and non-boundary annotations, respectively. $Y = Y_- \cup Y_+$ contains the indices of all pixels. This base model is modeled after HED [56] and performs similarly.

Semantic Segmentation For semantic segmentation, we train a model using K -way cross-entropy loss as in [6, 32]:

$$\ell_{semantic} = - \sum_i \sum_{c=1}^K 1_{[y_i=c]} \cdot \log(C_i) \quad (8)$$

where C_i is the class prediction (from a softmax transform) at pixel i , and y_i is the ground-truth class label.

Monocular Depth Estimation For monocular depth estimation, we use combined L_2 and L_1 losses to compare the predicted and ground-truth depth maps \mathbf{D} and $\hat{\mathbf{D}}$ which are on a log scale:

$$\ell_{depth} = \sum_{i=1} \|\mathbf{D}_i - \hat{\mathbf{D}}_i\|_2^2 + \gamma \|\mathbf{D}_i - \hat{\mathbf{D}}_i\|_1 \quad (9)$$

where $\gamma = 2$ controls the relative importance of the two losses. This mixed loss penalizes large errors quadratically (the L_2 term) while still assuring a non-vanishing gradient that continues to drive down small errors (the L_1 term). The idea behind our loss is similar to the reverse Huber loss as used in [35], which can be understood as concatenation of truncated \mathcal{L}_2 and \mathcal{L}_1 loss. However, the reverse Huber loss requires specifying a hyper-parameter for the boundary between \mathcal{L}_2 and \mathcal{L}_1 ; we find our mixed loss is robust and performs well with $\gamma \in [1, 5]$.

Surface Normal Estimation To predict surface normals, we insert a final L_2 normalization layer so that predicted normals have unit Euclidean length. In the literature, cosine distance is often used in the loss function to train the model, while performance metrics for normal estimation measure

²As MatConvNet itself does not provide perforated convolution, we release the code and models implemented with multiplicative gating at <https://github.com/aimerykong/Pixel-Attentional-Gating>.

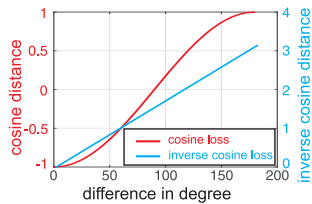


Figure 4: Inverse cosine loss has a constant gradient, while the gradient of the widely used cosine loss decreases as the prediction errors become small, preventing further model refinement.

the angular difference between prediction \mathbf{n} and the target normal $\hat{\mathbf{n}}$ [17, 13]. We address this discrepancy by incorporating inverse cosine distance along with cosine distance as our objective function:

$$\ell_{normal} = \sum_i -\mathbf{n}_i^T \hat{\mathbf{n}}_i + \lambda \cos^{-1}(\mathbf{n}_i^T \hat{\mathbf{n}}_i) \quad (10)$$

where λ controls the importance of the two part and we set $\lambda = 4$ throughout our experiments. Fig. 4 compares the curves of the two losses, and we can clearly see that the inverse cosine loss always produce meaningful gradients, whereas the popular cosine loss has “vanishing gradient” issue when prediction errors become small (analogous to the mixed L_1/L_2 loss for depth).

5. Experiments

To evaluate our method based on PAG, we choose datasets that span a variety of per-pixel labeling tasks, including boundary detection, semantic segmentation, depth and surface normal estimation. We first describe the datasets, and then carry out experiments to determine the best architectural configurations to exploit PAG and measure compute-performance trade-offs. We then evaluate our best models on standard benchmarks and show our approach achieves state-of-the-art or competitive performance for pixel-labeling. Finally, we visualize the attentional maps from MultiPool and ponder maps, and demonstrate qualitatively that our models pay more “attention” to specific regions/pixels, especially on boundaries between regions, *e.g.* semantic segments, and regions with sharp change of depth and normal.

5.1. Datasets

We utilize the following benchmark datasets.

BSDS500 [1] is the most popular dataset for boundary detection. It provides a standard split [1, 56] of 300 train-val images and 200 test images.

NYUv2 [48] consists of 1,449 RGB-D indoor scene images of the resolution 640×480 which include color and pixel-wise depth obtained by a Kinect sensor. We use the ground-truth segmentation into 40 classes provided in [20] and a standard train/test split into 795 and 654 images, respectively. For surface normal estimation, we compute the normal as target from depth using the method in [48] by fitting least-squares planes to neighboring sets of points in the point cloud.

Table 1: Ablation study for where to insert the PAG-based MultiPool module. Experiments are from boundary detection and semantic segmentation on BSDS500 and NYUv2 dataset, measured by F -score ($F_{bnd.}$) and IoU ($\text{IoU}_{seg.}$), respectively. Numbers are in % (higher is better).

metrics	base.	Res3	Res4	Res5	Res6	Res4-5	Res3-5	Res4-6	Res5-6
$F_{bnd.}$	79.00	79.19	79.19	79.14	—	79.18	79.07	—	—
$\text{IoU}_{seg.}$	42.05	44.13	45.67	46.52	45.99	45.48	44.83	44.97	46.44

Table 2: Performance comparison w.r.t computational parsimony controlled by hyper-parameter ρ on NYUv2 dataset for semantic segmentation.

param.&FLOPs	truncated		layer-skipping		perforatedCNN		MP@Res5 (PAG)		
ρ	$\times 10^{10}$	IoU	acc.	IoU	acc.	IoU	acc.	IoU	acc.
0.5	6.29	36.30	67.36	37.78	67.31	37.37	66.76	40.89	69.44
0.7	8.27	37.69	67.44	39.84	69.00	40.09	68.78	43.61	71.41
0.9	8.95	40.29	69.66	41.27	70.01	42.94	70.94	45.75	72.93
1.0	9.63	—	—	—	—	—	—	46.52	73.50

Stanford-2D-3D [3] contains 1,559 RGB panoramic images with depths, surface normal and semantic annotations covering six large-scale indoor areas from three different buildings. We use area 3 and 4 as a validation set (489 panoramas) and the remaining four areas for training (1,070 panoramas). The panoramas are very large (2048×4096) and contain black void regions at top and bottom due to the spherical panoramic topology. We rescale them by 0.5 and crop out the central two-thirds ($y \in [160, 863]$) resulting in final images of size 704×2048 -pixels. We randomly crop out sub-images of 704×704 resolution for training. Note that the surface normals in panoramic images are relative to the global coordinate system which cannot be determined from the image alone. Thus we transformed this global normal into local normal specified relative to the camera viewing direction (details in supplementary material). Note that such relative normals are also useful in scene understanding and reconstruction.

Cityscapes [10] contains high-quality pixel-level annotations of images collected in street scenes from 50 different cities. We use the standard split of training set (2,975 images) and validation set (500 images) for testing, respectively, labeled for 19 semantic classes as well as depth obtained by disparity. The images are of high resolution (1024×2048), and we randomly crop out sub-images of 800×800 resolution during training.

5.2. Analysis of Pixel-wise Attentional Gating

We evaluate different configurations of PAG on the BSDS500 and NYUv2 datasets for boundary detection and semantic segmentation (similar observations hold on other tasks, see supplementary materials). The goal of these experiments is to establish:

1. whether our base model is comparable to state-of-the-art methods;

- where to insert the PAG-based MultiPool module for the best performance;
- how our PAG-based method for computational parsimony impacts performance, and how it performs compared with other related methods, *e.g.* truncated ResNet and methods learning to skip/drop layers.

Base models: We train our base models as described in Section 4 without PAG units. The performance of our base model is on-par with state-of-the-art systems, achieving $\text{IoU}=42.05\%$ on NYUv2 for semantic segmentation (RefineNet [37] achieves $\text{IoU}=44.5$ with multi-resolution input), and $F = 0.79$ on BSDS500 for boundary detection (HED [56] achieves $F = 0.78$). More comprehensive comparisons with other related methods are shown later in Section 5.3.

MultiPool: Table 1 explores the effect of inserting the MultiPool operation at different layers in the base model. In Table 1, Res6 means that we insert MultiPool module in the additional convolutional layers above the ResNet50 base. For boundary detection, we do not initialize more convolutional layers above the backbone, so there is no Res6. For both tasks, we observe that including a PAG-based MultiPool module improves performance, but including more than one MultiPool module does not offer further improvements. We find inserting MultiPool module at second last macro residual block (Res4 or Res5 depending on task) yields the largest gain.

For semantic segmentation, our MultiPool also outperforms the weighted pooling in [32], which uses the same ResNet50 base. We conjecture this is due to three reasons. First, we apply the deconvolutional layer way before the last convolutional layer for softmax input as explained in Section 4.1. This increases resolution that enables the model to see better the fine details. Additionally, our set of pooling regions includes finer scales (rather than using powers of 2). Finally, the results in Table 4 show that PAG with binary masks performs slightly better ($\text{IoU}=46.5$ vs. $\text{IoU}=46.3$) than the (softmax) weighted average operation used in [32].

Computation-Performance Tradeoffs: Lastly, we evaluate how our dynamic parsimonious computation setup impacts performance and performs compared with other baselines. We show results of semantic segmentation on NYUv2 dataset in Table 2, comparing different baselines and our models with MultiPool at macro block Res5, $MP@Res5$ (PAG) for short, which are trained with different target computational budgets (specified by ρ). The “truncated” baseline means we simply remove top layers of ResNet to save computation, while “layer-skipping” is an implementation of [51] that learns to dynamically skip a subset of layer. “PerforatedCNN” is our implementation of [16] that matches the computational budget using a learned constant gating function (not dependent on input image). For fair comparison, we insert MultiPool module at the top of all

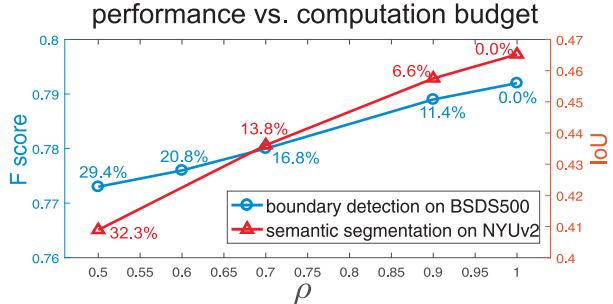


Figure 5: Performance vs. computation budget (controlled by ρ) for boundary detection and semantic segmentation, with saved computation (%) compared to full model as indicated by percentage number.

Table 3: Comparison with the state-of-the-art methods for boundary detection on BSDS500 dataset.

method	MP@Res4 [56]	HED [41]	COB [44]	LEP [44]	MCG [2]	MShift [9]	gPb-UCM [1]	NCut [47]	EGB [14]
odsF	0.792	0.780	0.793	0.757	0.747	0.601	0.726	0.641	0.636
oisF	0.806	0.796	0.820	0.793	0.779	0.644	0.760	0.674	0.674
AP	0.832	0.834	0.859	0.828	0.759	0.493	0.727	0.447	0.581

the compared methods. These results clearly suggest that the PAG approach outperforms all these methods, demonstrating that learning dynamic computation path at the pixel level is helpful for per-pixel labeling tasks. It is also worth noting that PerforatedCNN does not support fully convolutional computation requiring that the input image have a fixed size in order to learn fixed computation paths over the image. In contrast, our method is fully convolutional that is able to take as input images of arbitrary size and perform computing with input-dependent dynamic paths.

Fig. 5 shows that, as we decrease the computation budget, the performance of the PAG-based method degrades gracefully even as the amount of computation is scaled back to 70%, merely inducing 2.4% and 5.6% performance degradation on boundary detection and semantic segmentation compared to their full model, *i.e.*, $F=0.773$ vs. $F=0.792$ and $\text{IoU}=0.409$ vs. $\text{IoU}=0.465$. Table 2 highlights the comparison to truncation and layer-skipping models adjusted to match the same computational budget as PAG. For these approaches, performance decays much more sharply with decreasing budget. These results also highlight that the target sparsity parameter ρ provides tight control over the actual average computation of the model.

5.3. Comprehensive Benchmark Comparison

We now compare our models under different degrees of computational parsimony ($\rho=\{0.5, 0.7, 0.9, 1.0\}$) with other state-of-the-art systems for pixel labeling.

Taking boundary detection as the first task, we quantitatively compare our model to COB [41], HED [56], gPb-UCM [1], LEP [44], UCM [1], NCuts [47], EGB [14], MCG [2] and the mean shift (MShift) algorithm [9]. Table 3

Table 4: Semantic segmentation is measured by Intersection over Union (IoU), pixel accuracy (acc), and iIoU that leverages the size of segments w.r.t categories. Results marked by † are from our trained models with the released code.

methods/metrics	NYUv2 [48]		Stanford-2D-3D [3]		Cityscapes [48]	
	IoU	pixel acc.	IoU	pixel acc.	IoU	iIoU
baseline	42.1	71.1	79.5	92.1	73.8	54.7
MP@Res5 (w-Avg.)	46.3	73.4	83.7	93.6	75.8	56.9
MP@Res5 (PAG)	46.5	73.5	83.7	93.7	75.7	55.8
MP@Res5 ($\rho=0.9$)	45.8	72.9	82.8	93.3	75.0	55.4
MP@Res5 ($\rho=0.7$)	43.6	71.4	82.4	93.2	72.6	55.1
MP@Res5 ($\rho=0.5$)	40.9	69.4	81.8	92.9	70.8	53.2
PerspectiveParsing [32]	44.5	72.1	76.5	91.0	75.4	56.8
DeepLab [6]	—	—	69.8 [†]	88.0 [†]	71.4	51.6
LRR [18]	—	—	—	—	70.0	48.0
PSPNet [58]	—	—	67.4 [†]	87.6 [†]	78.7	60.4
RefineNet-Res50 [37]	43.8	—	—	—	—	—
RefineNet-Res152 [37]	46.5	73.6	—	—	—	—

Table 5: Depth estimation is measured by standard threshold accuracy, *i.e.* the percentage (%) of predicted pixel depths d_i s.t. $\delta = \max(\frac{d_i}{\hat{d}_i}, \frac{\hat{d}_i}{d_i}) < \tau$, where $\tau = \{1.25, 1.25^2, 1.25^3\}$. Methods with * use $\sim 100k$ extra images to train.

methods/metric	NYUv2 [48]			Stanford-2D-3D [3]			Cityscapes [48]		
	1.25	1.25 ²	1.25 ³	1.25	1.25 ²	1.25 ³	1.25	1.25 ²	1.25 ³
baseline	71.1	93.2	98.5	73.1	92.1	97.5	29.0	53.8	75.8
MP@Res5 (w-Avg.)	74.5	94.4	98.8	77.5	94.1	97.9	33.7	63.9	76.9
MP@Res5 (PAG)	75.1	94.4	98.8	77.6	94.1	97.9	34.6	66.2	77.2
MultiPool ($\rho=0.9$)	74.5	94.4	98.8	77.3	93.9	97.8	34.5	63.7	76.9
MultiPool ($\rho=0.7$)	71.0	93.3	98.5	75.4	92.8	97.6	32.0	63.5	75.8
MultiPool ($\rho=0.5$)	67.3	91.0	97.7	72.7	91.3	97.1	28.7	58.7	71.6
Liu [35]	61.4	88.3	97.1	—	—	—	—	—	—
Ladicky* [33]	54.2	82.9	94.0	—	—	—	—	—	—
Eigen* [13]	61.4	88.8	97.2	—	—	—	—	—	—
Eigen* [12]	76.9	95.0	98.8	—	—	—	—	—	—
Laina* [35]	81.1	95.3	98.8	—	—	—	—	—	—

shows comparison to all the methods (PR curves in supplementary material), demonstrating our model achieves state-of-the-art performance. Note that our model has the same backbone architecture of HED [56], but outperforms it with our MultiPool module which increases receptive fields at higher levels. Our model performs on par with COB [41], which uses auxiliary losses for oriented boundary detection. Note that it is possible to surpass human performance with sophisticated techniques [29], but we don’t pursue this as it is out the scope of this paper.

Table 4, 5 and 6 show the comprehensive comparisons on the tasks of semantic segmentation, monocular depth and surface normal estimation, respectively. In addition to comparing with state-of-the-art methods, we also show the result of MultiPool module with softmax weighted average operation, termed by *MP@Res5 (w-Avg.)*. Interestingly, MultiPool performs slightly better when equipped with PAG than the weighted average fusion. We attribute this to the facts that, longer training has been done in the stage-wise training strategy, and PAG unit also constrains the information flow to train specific branches.

Our baseline model achieves performance on par with recent methods for all tasks. When inserting the MultiPool module, we improve even further and surpass the compared methods for most tasks and datasets. In particular, on datasets with large perspective images, *i.e.* Stanford-2D-3D

Table 6: Surface normal estimation is measured by mean angular error and the percentage of prediction error within t° degree where $t = \{11.25, 22.50, 30.00\}$. Smaller ang. err. means better performance as marked by \downarrow .

methods/metrics	NYUv2 [48]				Stanford-2D-3D [3]			
	ang. err. \downarrow	11.25 $^\circ$	22.50 $^\circ$	30.00 $^\circ$	ang. err. \downarrow	11.25 $^\circ$	22.50 $^\circ$	30.00 $^\circ$
baseline	22.3	34.4	62.5	74.4	19.0	51.5	68.6	76.3
MP@Res5 (w-Avg.)	21.9	35.9	63.8	75.3	16.5	58.2	74.2	80.4
MP@Res5 (PAG)	21.7	36.1	64.2	75.5	16.5	58.3	74.2	80.4
MP@Res5 ($\rho=0.9$)	21.9	35.9	63.9	75.4	16.7	57.5	73.7	80.1
MP@Res5 ($\rho=0.7$)	22.5	34.7	62.5	74.1	17.0	56.5	73.1	79.7
MP@Res5 ($\rho=0.5$)	23.6	31.9	59.7	71.8	17.7	54.7	71.4	78.5
Fouhey [17]	35.3	16.4	36.6	48.2	—	—	—	—
Ladicky [34]	35.5	24.0	45.6	55.9	—	—	—	—
Wang [53]	28.8	35.2	57.1	65.5	—	—	—	—
Eigen [12]	22.2	38.6	64.0	73.9	—	—	—	—

and Cityscapes, the MultiPool module shows greater improvement. Reducing the computation 20-30% only yields a performance drop of 3-5% generally.

For depth and surface normal estimation tasks, our baseline models also perform very well. This is notable since we don’t leverage multi-task learning (unlike Eigen [12]) and do not use extra images to augment training set (unlike most methods for depth estimation using $\sim 100k$ extra images to augment the training set as shown in Table 5). We attribute this to the combination of the proposed PAG MultiPool and carefully designed losses for depth and surface normal estimation.

5.4. Qualitative Visualization

We visualize the prediction and attention maps in Fig. 1 for the four datasets, respectively. We find that the binary attention maps are qualitatively similar across layers and hence summarize them with a “ponder map” by summing maps across layers (per-layer maps can be found in the supplementary material). We can see our models allocate more computation on the regions/pixels which are likely sharp transitions, *e.g.* boundaries between semantic segments, depth discontinuities and normal discontinuities (*e.g.* between wall and ceiling).

6. Conclusion and Future Work

In this paper, we have studied the problem of dynamic inference for pixel labeling tasks under limited computation budget with a deep CNN network. To achieve this, we propose a Pixel-wise Attentional Gating unit (PAG) that learns to generate sparse binary masks that control computation at each layer on a per-pixel basis. Our approach differs from previous methods in demonstrating improved performance on pixel labeling tasks using spatially varying computation trained with simple task-specific loss. This makes our approach a good candidate for general use as it is agnostic to tasks and architectures, and avoids more complicated reinforcement learning-style approaches, instead relying on a simple, easy-to-set sparsity target that correlates closely with empirical computational cost. As our PAG is based on a generic attention mechanism, we anticipate future work

might explore task-driven constraints for further improvements and savings.

Acknowledgement This project is supported by NSF grants IIS-1618806, IIS-1253538, a hardware donation from NVIDIA and Google Graduate Research Award.

References

- [1] P. Arbelaez, M. Maire, C. Fowlkes, and J. Malik. Contour detection and hierarchical image segmentation. *IEEE Transactions on Pattern Analysis and Machine Intelligence (PAMI)*, 33(5):898–916, 2011.
- [2] P. Arbeláez, J. Pont-Tuset, J. T. Barron, F. Marques, and J. Malik. Multiscale combinatorial grouping. In *Proceedings of the IEEE Conference on Computer Vision and Pattern Recognition (CVPR)*, pages 328–335, 2014.
- [3] I. Armeni, S. Sax, A. R. Zamir, and S. Savarese. Joint 2d-3d-semantic data for indoor scene understanding. In *Proceedings of the IEEE International Conference on Computer Vision (ICCV)*, 2017.
- [4] A. Bansal, B. Russell, and A. Gupta. Marr revisited: 2d-3d alignment via surface normal prediction. In *Proceedings of the IEEE Conference on Computer Vision and Pattern Recognition (CVPR)*, pages 5965–5974, 2016.
- [5] M. A. Carreira-Perpinán and Y. Idelbayev. Model compression as constrained optimization, with application to neural nets. *Part III: Pruning*. *arXiv*, 2017.
- [6] L.-C. Chen, G. Papandreou, I. Kokkinos, K. Murphy, and A. L. Yuille. Deeplab: Semantic image segmentation with deep convolutional nets, atrous convolution, and fully connected crfs. *IEEE Transactions on Pattern Analysis and Machine Intelligence (PAMI)*, 2016.
- [7] L.-C. Chen, Y. Yang, J. Wang, W. Xu, and A. L. Yuille. Attention to scale: Scale-aware semantic image segmentation. In *Proceedings of the IEEE conference on Computer Vision and Pattern Recognition (CVPR)*, pages 3640–3649, 2016.
- [8] S. Chetlur, C. Woolley, P. Vandermersch, J. Cohen, J. Tran, B. Catanzaro, and E. Shelhamer. cudnn: Efficient primitives for deep learning. *arXiv preprint arXiv:1410.0759*, 2014.
- [9] D. Comaniciu and P. Meer. Mean shift: A robust approach toward feature space analysis. *IEEE Transactions on Pattern Analysis and Machine Intelligence (PAMI)*, 24(5):603–619, 2002.
- [10] M. Cordts, M. Omran, S. Ramos, T. Rehfeld, M. Enzweiler, R. Benenson, U. Franke, S. Roth, and B. Schiele. The cityscapes dataset for semantic urban scene understanding. In *Proceedings of the IEEE Conference on Computer Vision and Pattern Recognition (CVPR)*, pages 3213–3223, 2016.
- [11] J. Deng, W. Dong, R. Socher, L.-J. Li, K. Li, and L. Fei-Fei. Imagenet: A large-scale hierarchical image database. In *Proceedings of the IEEE Conference on Computer Vision and Pattern Recognition (CVPR)*, pages 248–255. IEEE, 2009.
- [12] D. Eigen and R. Fergus. Predicting depth, surface normals and semantic labels with a common multi-scale convolutional architecture. In *Proceedings of the IEEE International Conference on Computer Vision (ICCV)*, pages 2650–2658, 2015.
- [13] D. Eigen, C. Puhrsch, and R. Fergus. Depth map prediction from a single image using a multi-scale deep network. In *Advances in Neural Information Processing Systems (NIPS)*, 2014.
- [14] P. F. Felzenszwalb and D. P. Huttenlocher. Efficient graph-based image segmentation. *International Journal of Computer Vision (IJCV)*, 59(2):167–181, 2004.
- [15] M. Figurnov, M. D. Collins, Y. Zhu, L. Zhang, J. Huang, D. Vetrov, and R. Salakhutdinov. Spatially adaptive computation time for residual networks. In *Proceedings of the IEEE Conference on Computer Vision and Pattern Recognition (CVPR)*, 2017.
- [16] M. Figurnov, A. Ibraimova, D. P. Vetrov, and P. Kohli. Perforatedcnns: Acceleration through elimination of redundant convolutions. In *Advances in Neural Information Processing Systems (NIPS)*, pages 947–955, 2016.
- [17] D. F. Fouhey, A. Gupta, and M. Hebert. Data-driven 3d primitives for single image understanding. In *IEEE International Conference on Computer Vision (ICCV)*, pages 3392–3399. IEEE, 2013.
- [18] G. Ghiasi and C. C. Fowlkes. Laplacian pyramid reconstruction and refinement for semantic segmentation. In *European Conference on Computer Vision (ECCV)*, 2016.
- [19] E. J. Gumbel. *Statistics of extremes*. Courier Corporation, 2012.
- [20] S. Gupta, P. Arbelaez, and J. Malik. Perceptual organization and recognition of indoor scenes from rgb-d images. In *Proceedings of the IEEE Conference on Computer Vision and Pattern Recognition (CVPR)*, 2013.
- [21] S. Han, H. Mao, and W. J. Dally. Deep compression: Compressing deep neural networks with pruning, trained quantization and huffman coding. In *International Conference on Learning Representations (ICLR)*, 2016.
- [22] K. He, X. Zhang, S. Ren, and J. Sun. Deep residual learning for image recognition. In *Proceedings of the IEEE Conference on Computer Vision and Pattern Recognition (CVPR)*, pages 770–778, 2016.
- [23] G. Hinton, O. Vinyals, and J. Dean. Distilling the knowledge in a neural network. In *NIPS Workshop in Deep Learning and Representation Learning*, 2015.
- [24] G. Huang, Z. Liu, K. Q. Weinberger, and L. van der Maaten. Densely connected convolutional networks. In *Proceedings of the IEEE conference on Computer Vision and Pattern Recognition (CVPR)*, 2017.
- [25] G. Huang, Y. Sun, Z. Liu, D. Sedra, and K. Q. Weinberger. Deep networks with stochastic depth. In *European Conference on Computer Vision (ECCV)*, pages 646–661. Springer, 2016.
- [26] F. N. Iandola, S. Han, M. W. Moskewicz, K. Ashraf, W. J. Dally, and K. Keutzer. Squeezenet: Alexnet-level accuracy with 50x fewer parameters and <0.5 mb model size. In *International Conference on Learning Representations (ICLR)*, 2017.
- [27] S. Ioffe and C. Szegedy. Batch normalization: Accelerating deep network training by reducing internal covariate shift. In *International Conference on Machine Learning (ICML)*, pages 448–456, 2015.

- [28] E. Jang, S. Gu, and B. Poole. Categorical reparameterization with gumbel-softmax. In *International Conference on Learning Representations (ICLR)*, 2017.
- [29] I. Kokkinos. Pushing the boundaries of boundary detection using deep learning. In *International Conference on Learning Representations (ICLR)*, 2016.
- [30] S. Kong and C. Fowlkes. Low-rank bilinear pooling for fine-grained classification. In *2017 IEEE Conference on Computer Vision and Pattern Recognition (CVPR)*, pages 7025–7034. IEEE, 2017.
- [31] S. Kong and C. Fowlkes. Recurrent pixel embedding for instance grouping. In *Proceedings of the IEEE conference on Computer Vision and Pattern Recognition (CVPR)*, 2017.
- [32] S. Kong and C. Fowlkes. Recurrent scene parsing with perspective understanding in the loop. In *Proceedings of the IEEE conference on Computer Vision and Pattern Recognition (CVPR)*, 2018.
- [33] L. Ladicky, J. Shi, and M. Pollefeys. Pulling things out of perspective. In *Proceedings of the IEEE Conference on Computer Vision and Pattern Recognition (CVPR)*, 2014.
- [34] L. Ladicky, B. Zeisl, and M. Pollefeys. Discriminatively trained dense surface normal estimation. In *European Conference on Computer Vision (ECCV)*, pages 468–484. Springer, 2014.
- [35] I. Laina, C. Rupprecht, V. Belagiannis, F. Tombari, and N. Navab. Deeper depth prediction with fully convolutional residual networks. In *International Conference on 3D Vision (3DV)*, pages 239–248. IEEE, 2016.
- [36] B. Li, C. Shen, Y. Dai, A. van den Hengel, and M. He. Depth and surface normal estimation from monocular images using regression on deep features and hierarchical crfs. In *Proceedings of the IEEE Conference on Computer Vision and Pattern Recognition (CVPR)*, pages 1119–1127, 2015.
- [37] G. Lin, A. Milan, C. Shen, and I. Reid. Refinenet: Multi-path refinement networks with identity mappings for high-resolution semantic segmentation. In *Proceedings of the IEEE Conference on Computer Vision and Pattern Recognition (CVPR)*, 2017.
- [38] F. Liu, C. Shen, and G. Lin. Deep convolutional neural fields for depth estimation from a single image. In *Proceedings of the IEEE Conference on Computer Vision and Pattern Recognition (CVPR)*, pages 5162–5170, 2015.
- [39] C. J. Maddison, A. Mnih, and Y. W. Teh. The concrete distribution: A continuous relaxation of discrete random variables. In *International Conference on Learning Representations (ICLR)*, 2017.
- [40] A. Mallya and S. Lazebnik. Packnet: Adding multiple tasks to a single network by iterative pruning. In *Proceedings of the IEEE Conference on Computer Vision and Pattern Recognition (CVPR)*, 2018.
- [41] K.-K. Maninis, J. Pont-Tuset, P. Arbelaez, and L. Van Gool. Convolutional oriented boundaries: From image segmentation to high-level tasks. *IEEE Transactions on Pattern Analysis and Machine Intelligence (PAMI)*, 2017.
- [42] P. Molchanov, S. Tyree, T. Karras, T. Aila, and J. Kautz. Pruning convolutional neural networks for resource efficient inference. In *International Conference on Learning Representations (ICLR)*, 2017.
- [43] V. Nair and G. E. Hinton. Rectified linear units improve restricted boltzmann machines. In *International Conference on Machine Learning (ICML)*, pages 807–814, 2010.
- [44] L. Najman and M. Schmitt. Geodesic saliency of watershed contours and hierarchical segmentation. *IEEE Transactions on Pattern Analysis and Machine Intelligence (PAMI)*, 18(12):1163–1173, 1996.
- [45] K. Ovtcharov, O. Ruwase, J.-Y. Kim, J. Fowers, K. Strauss, and E. S. Chung. Accelerating deep convolutional neural networks using specialized hardware. *Microsoft Research Whitepaper*, 2(11), 2015.
- [46] N. Shazeer, A. Mirhoseini, K. Maziarz, A. Davis, Q. Le, G. Hinton, and J. Dean. Outrageously large neural networks: The sparsely-gated mixture-of-experts layer. In *International Conference on Learning Representations (ICLR)*, 2017.
- [47] J. Shi and J. Malik. Normalized cuts and image segmentation. *IEEE Transactions on Pattern Analysis and Machine Intelligence (PAMI)*, 22(8):888–905, 2000.
- [48] N. Silberman, D. Hoiem, P. Kohli, and R. Fergus. Indoor segmentation and support inference from rgb-d images. In *European Conference on Computer Vision (ECCV)*, pages 746–760. Springer, 2012.
- [49] K. Simonyan and A. Zisserman. Very deep convolutional networks for large-scale image recognition. In *International Conference on Learning Representations (ICLR)*, 2015.
- [50] A. Vedaldi and K. Lenc. Matconvnet: Convolutional neural networks for matlab. In *Proceedings of the 23rd ACM International Conference on Multimedia*, pages 689–692. ACM, 2015.
- [51] A. Veit and S. Belongie. Convolutional networks with adaptive computation graphs. In *European Conference on Computer Vision (ECCV)*, 2018.
- [52] A. Veit, M. J. Wilber, and S. Belongie. Residual networks behave like ensembles of relatively shallow networks. In *Advances in Neural Information Processing Systems (NIPS)*, pages 550–558, 2016.
- [53] X. Wang, D. Fouhey, and A. Gupta. Designing deep networks for surface normal estimation. In *Proceedings of the IEEE Conference on Computer Vision and Pattern Recognition (CVPR)*, pages 539–547, 2015.
- [54] X. Wang, F. Yu, Z.-Y. Dou, and J. E. Gonzalez. Skipnet: Learning dynamic routing in convolutional networks. In *European Conference on Computer Vision (ECCV)*, 2018.
- [55] Z. Wu, T. Nagarajan, A. Kumar, S. Rennie, L. S. Davis, K. Grauman, and R. Feris. Blockdrop: Dynamic inference paths in residual networks. In *Proceedings of the IEEE Conference on Computer Vision and Pattern Recognition (CVPR)*, 2017.
- [56] S. Xie and Z. Tu. Holistically-nested edge detection. In *Proceedings of the IEEE International Conference on Computer Vision (ICCV)*, pages 1395–1403, 2015.
- [57] F. Yu and V. Koltun. Multi-scale context aggregation by dilated convolutions. In *International Conference on Learning Representations (ICLR)*, 2016.
- [58] H. Zhao, J. Shi, X. Qi, X. Wang, and J. Jia. Pyramid scene parsing network. In *Proceedings of the IEEE Conference on Computer Vision and Pattern Recognition (CVPR)*, 2017.

Pixel-wise Attentional Gating for Scene Parsing

(Appendix)

Abstract

In the supplementary material, we first present in detail how to transform the (unpredictable) global surface normals into (predictable) local normals in panoramic images. We then show more ablation studies on the loss functions introduced in the main paper and MultiPool module with/without PAG unit. Finally, we provide more qualitative visualization of the results for various pixel-labeling tasks, as well as the attentional ponder maps and MultiPool maps.

1. Local Surface Normal in Panoramas

Stanford-2D-3D [3] provides cylindrical panoramas with global surface normals, which are in a global Earth-Centered-Earth-Fixed coordinate system (ECEF). For example, the normals for a wall have the same direction pointing to the true north. However, such global coordinate system is impossible to determine from a single image, and thus the global normals are unpredictable purely based on panoramic image data alone. For this reason, we propose to transform the global normals into “local normals” which are relative to the camera viewing direction. We note that such a predictability makes relative normals more useful in scene understanding and reconstruction.

For a cylindrical panorama, we assume the vertical axis of the panorama is aligned with the global coordinate frame. Given a global normal at a pixel $\mathbf{n} = [x, y, z]^T$, we can apply a rotation matrix \mathbf{R} in the horizontal plane (x and y) to obtain its local normal $[x', y', z]^T$ in the “camera viewing” coordinate system:

$$\begin{bmatrix} x' \\ y' \\ z \end{bmatrix} = \begin{bmatrix} \mathbf{R}, \mathbf{0} \\ \mathbf{0}, 1 \end{bmatrix} \begin{bmatrix} x \\ y \\ z \end{bmatrix} \quad (11)$$

where z is the variable for vertical direction.

We would like to determine the appropriate rotation matrices for all pixels where each pixel has its own rotation matrix which is controlled by a single signed angle parameter θ . For a cylindrical panorama, the relative difference in viewing direction between two image locations is completely specified by their horizontal separation in image coordinates. Therefore, to determine the set of rotations, we simply need to specify an origin for which the rotation is $\theta = 0$, i.e., a canonical point whose surface normal points exactly to the camera. Given the rotation matrix for the canonical point, the rotation angle for remaining points can

be calculated as $2\pi \frac{\Delta W}{W}$, where W is the width of panorama and ΔW is the offset from the target pixel to the canonical pixel (with sign). Fig. 6 illustrates the principle behind our methodology.

We note that it is straightforward to identify canonical points manually by choosing a flat vertical surface (e.g., a wall) and selecting the point on it which is nearest to the camera (e.g. shape of panoramic topology). An automated method can be built with the same rule based on semantic annotation and depth map. However, the automated method may suffer from cluttered scene (e.g. boards and bookcase on the wall), yet such manual annotation enables us to visualize what the local normals would look like if we clicked the “wrong” points³. From the three random panoramic images as shown in Fig. 7, we can see such canonical points lie in the color bands (manually drawn for demonstration) noted in the figure. They are easy to detect by eye based on the warping effect due to panoramic topology. We made an easy-to-use tool to click a canonical point for each panoramic image. Fig. 7 demonstrates the resulting transformed normals after an annotator has clicked on some point in the color band. We note that annotating each panoramic image costs less than 5 seconds, and it required less than three hours to carefully annotate all 1,559 panoramas in the dataset. We also compare the annotation when clicking on different canonical points (at different color bands) for the same image, and the maximum difference of normals for all spatial locations is only less than 8° degree. This means the annotation is easy and robust. We will release to public all the transformed local surface normals as an extension to Stanford-2D-3D dataset, as well as our interactive tool for annotation.

2. Further Analysis of Loss Functions and MultiPool Module

In this section, we describe further analysis on the architectural choices of where to insert the MultiPool module, as well as new loss functions introduced in our main paper. We conduct experiments on BSDS500 [1] and NYUv2 [12] datasets for boundary detection, depth and surface normal estimation, to complement the analysis in the main paper.

2.1. Boundary Detection on BSDS500 Dataset

In Fig. 8, we show the precision-recall curves for boundary detection on BSDS500 dataset [1]. First, Fig. 8 (a) summarizes our ablation study on where to insert the MultiPool module to obtain the largest performance gain. We observe that the best performance is achieved when the MultiPool module is inserted at the fourth macro building block (Res4), i.e. the second last macro block or the Resnet50

³Clicking on the “wrong” points will leads to some normals pointing outwards the camera.

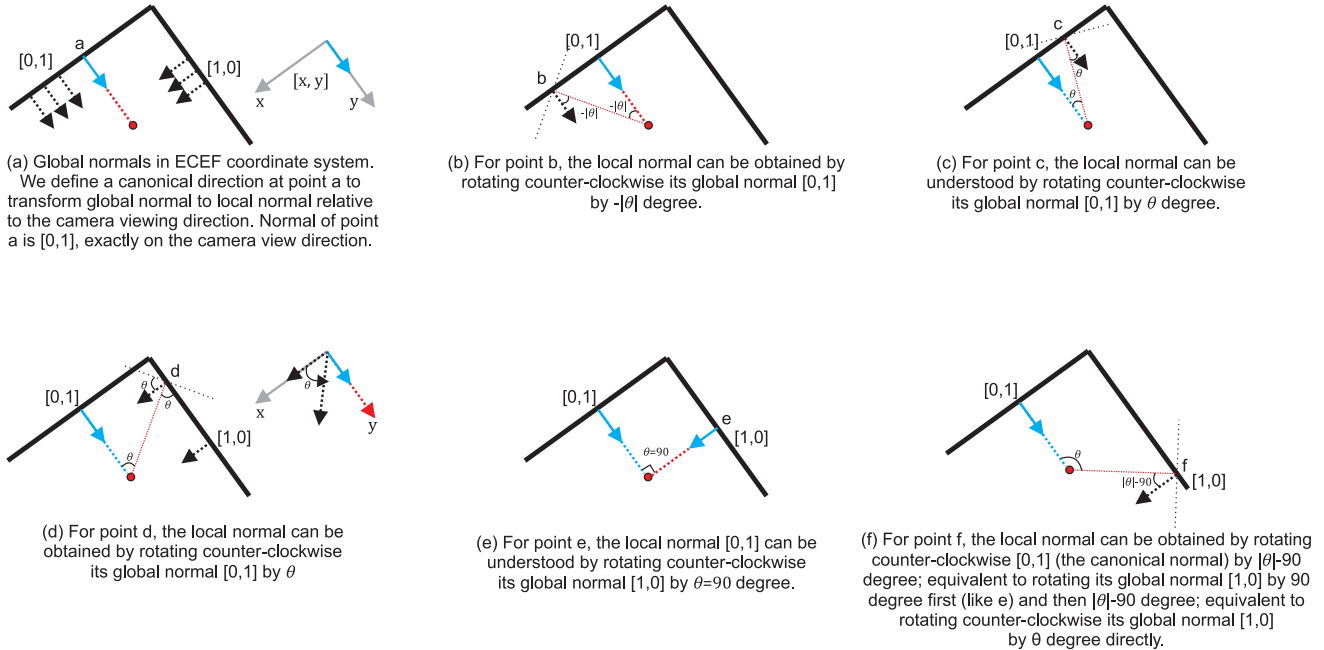


Figure 6: An illustration of how to transform global normals into local normals specified relative to the camera viewing direction. Global normals in Stanford-2D-3D dataset [3] are in Earth-Centered-Earth-Fixed (ECEF) coordinate system.

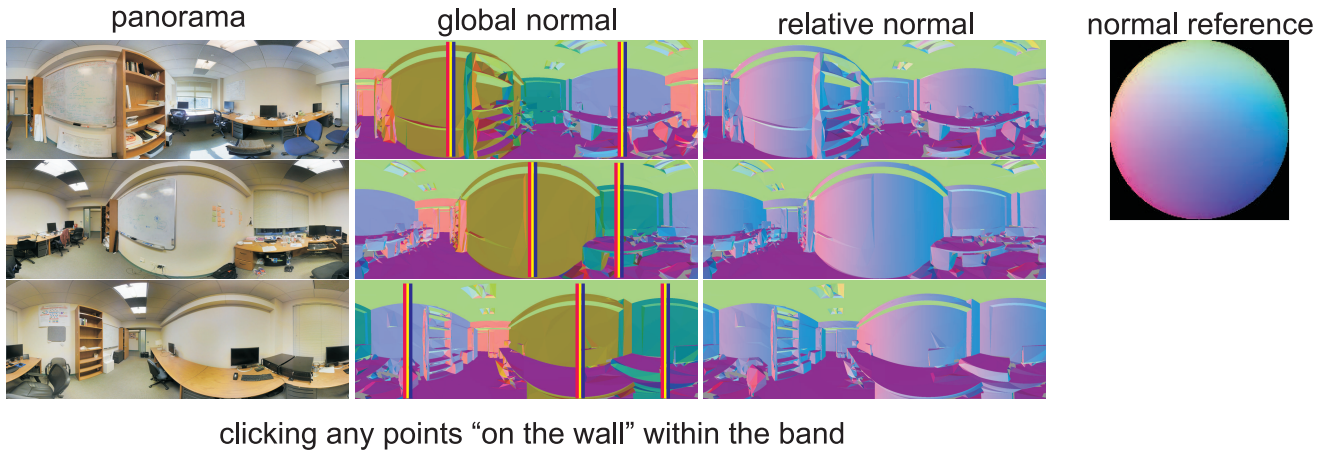


Figure 7: We draw the color bands on global normal maps to indicate points of the wall within these bands can be treated as canonical points, whose normals exactly face towards the camera. For a human annotator, these points can be easily detected by looking at the shape of the room. Our interface allows an annotator to click a point supposedly within any one of the bands, and through the coordinate transform, such global normals can be transformed into predictable, relative normals. The rightmost pie chart provides reference on the local surface normal relative to the camera viewing direction.

architecture. This supports our conclusion that MultiPool inserted at the second last macro building block leads to the largest performance gain.

Moreover, based on the “MultiPool@Res4” model, we gradually insert PAG units for parsimonious inference, and decrease the hyper-parameter ρ which controls the sparsity degree of binary masks (the sparser the masks are, the more parsimonious constraint is imposed). In particular, note that

$\rho = 0.5$ means $\sim 30\%$ computation has been saved, at which point our model achieves $F = 0.773$, only degrading by 2.4% performance. This shows that the ResNet50 model has sufficient capacity for boundary detection, and more parsimonious constraint does not harm the performance too much. Perhaps due to this reason, the MultiPool module does not improve performance remarkably for boundary detection.

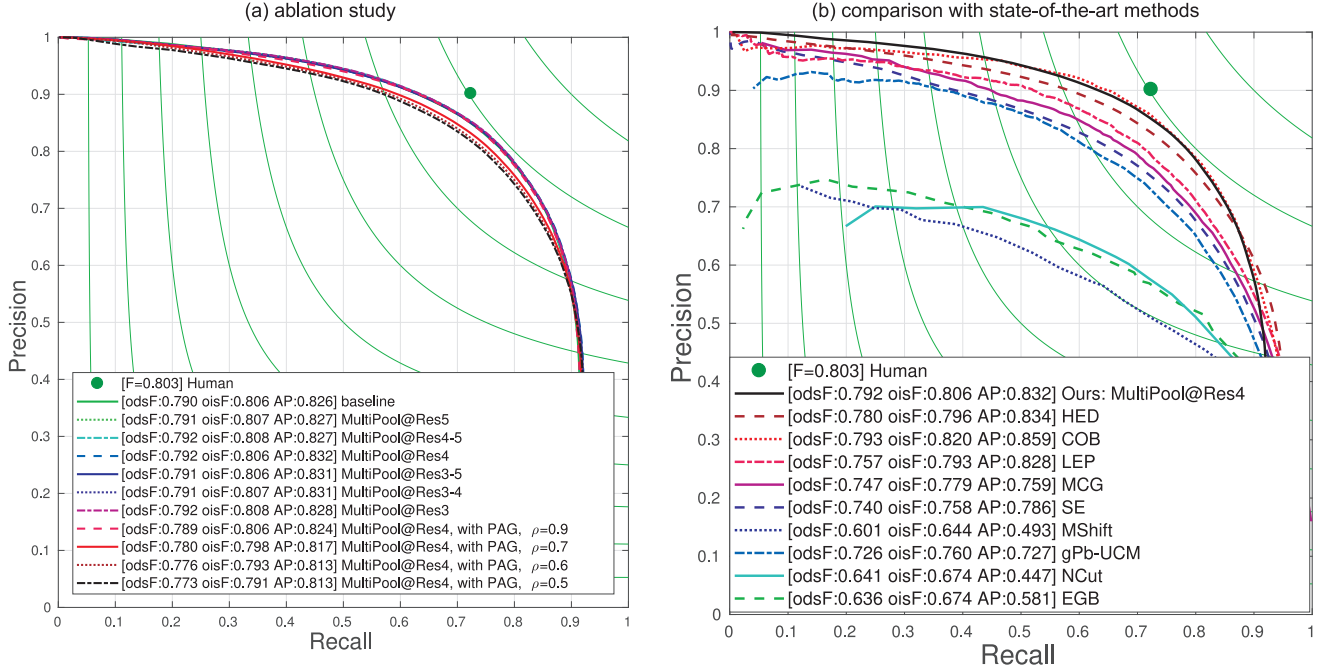


Figure 8: Precision-Recall curves on boundary detection on BSDS500 dataset. (a) Ablation study. (b) Comparison with state-of-the-art methods.

Finally, by comparing to state-of-the-art methods as shown in Fig. 8 (b), we note our “MultiPool@Res4” model outperforms HED [56] which shares the same architecture but without MultiPool module, and performs similarly with COB [41] which further exploits auxiliary loss for oriented boundary detection. This validates that the PAG-based MultiPool module improves performance by providing each pixel the “correct” size of pooling field.

2.2. Monocular Depth Estimation on NYUv2 Dataset

We provide complementary ablation study on the task of monocular depth estimation on NYUv2 dataset.

First, we study where to insert the MultiPool module to obtain the largest performance gain. We train our base model using $L2$ loss function only, and insert the MultiPool module (without PAG but the softmax weighted average operation) at each macro building block one by one. We list the performance of these models in Table 7. From the table, we observe that no matter where to insert the MultiPool module, it consistently improves the performance; while when MultiPool module is inserted at Res5, which is the second last macro building block, we obtain the largest performance gain. These observations, along with what reported in the main paper, support our conclusion that one is able to get the best performance when inserting the MultiPool module at the second last macro building block of a ResNet model.

Then, we study the loss function mixing $L1$ and $L2$ as introduced in the main paper. We train the models with MultiPool module inserted at the fifth macro block (MP@Res5), using different loss functions, and report the results in Table 8. It’s clear to see the mixed $L1$ and $L2$ loss leads to the best performance, especially on the metric of < 1.25 , focusing on the range of small prediction errors where $L2$ loss alone is unable to provide a meaningful gradient. Moreover, we compare the model between PAG-based MultiPool and that based on softmax weighted average operation in Table 8. Again, our PAG-based MultiPool not only outperforms the weighted-average MultiPool, but also maintains computation as well as memory storage because of the perforated convolution (selecting spatial locations to compute).

2.3. Surface Normal Estimation on NYUv2 Dataset

Similar to the ablation study for monocular depth estimation task, we study firstly how the proposed loss function improves performance, then where to insert the MultiPool module for the best performance, and lastly performance comparison between PAG-based and weighted-average MultiPool.

In Table 9, we compare the results from models trained with different loss functions. We can see the combination of cosine distance loss and the inverse cosine loss achieves the best performance. From the table, we clearly see that the improvement on metric 11.25° is more remarkable, which focuses on small prediction errors. This is because, as an-

Table 7: Ablation study of where to insert the MultiPool module to obtain the largest performance gain for monocular depth estimation on NYUv2 dataset. All models are evaluated over the standard split of NYUv2 dataset, with $L2$ loss only, and with softmax weighted average in the MultiPool module. The performance is measured by standard threshold accuracy, *i.e.* the percentage of predicted pixel depths d_i s.t. $\delta = \max(\frac{d_i}{\hat{d}_i}, \frac{\hat{d}_i}{d_i}) < \tau$, where $\tau = \{1.25, 1.25^2, 1.25^3\}$.

metrics	base.	MP@Res3	MP@Res4	MP@Res5	MP@Res6	MP@Res3-4	MP@Res5-6
1.25	0.711	0.721	0.726	0.737	0.725	0.726	0.726
1.25 ²	0.932	0.935	0.939	0.939	0.936	0.938	0.939
1.25 ³	0.985	0.986	0.986	0.986	0.985	0.986	0.985

Table 8: Ablation study of loss functions and PAG unit for monocular depth estimation on NYUv2 dataset. Our MP@Res5 model is the base model, unless specified, all the models are trained with softmax weighted average in the MultiPool module. The performance is measured by standard threshold accuracy, *i.e.* the percentage of predicted pixel depths d_i s.t. $\delta = \max(\frac{d_i}{\hat{d}_i}, \frac{\hat{d}_i}{d_i}) < \tau$, where $\tau = \{1.25, 1.25^2, 1.25^3\}$.

metrics	$L2$ loss	$L1$ loss	$L1+L2$ loss	$L1+L2$ loss (PAG)
1.25	0.737	0.743	0.745	0.751
1.25 ²	0.939	0.942	0.944	0.944
1.25 ³	0.986	0.987	0.988	0.988

alyzed in the main paper, the combined loss function provides meaningful gradient “everywhere”, whereas the cosine distance loss alone has “vanishing gradient” issue when the prediction errors become small.

We then study where to insert the MultiPool module to get the best performance in Table 10. Note that, in this ablation study, we didn’t use PAG for binary masks, but instead using weighted average based on softmax operator. Consistent to previous discovery, when inserting MultiPool at the second last macro block, we achieve the best performance. In Table 11, we compare the results with PAG-based MultiPool and weighted-average MultiPool. We conclude with consistent observation that PAG unit does not harm the performance compared to the softmax weighted average fusion, but instead achieves better performance with the same computation overhead, thanks to the perforated convolution.

3. More Qualitative Visualization

In this section, we visualize more results of boundary detection, semantic segmentation, monocular depth estimation and surface normal estimation, over the four datasets used in the paper, BSDS500 (Fig. 9), NYUv2 (Fig. 10), Stanford-2D-3D (Fig. 11) and Cityscapes (Fig. 12). In the figures, we show the ponder map for each macro building block, as well as the overall ponder map. From these ponder maps, we can see our model learns to dynamically allocate computation at different spatial location, primarily expending more computation on the regions/pixels which are regions with sharp changes, e.g. boundary between semantic segments, regions between two depth layer, loca-

tions around normal changes like between wall and ceiling. We also show all the binary maps produced by PAG units in Fig. 13 over a random image from Stanford2D3D dataset for semantic segmentation, surface normal estimation and depth estimation.

In Fig. 14, we visualize the learned binary masks by PerforatedCNN [16] on NYUv2 dataset for semantic segmentation. We also accumulate all the binary masks towards the ponder map, from which we can see that the active pixels largely follow uniform distribution. This is different from what reported in [16] that the masks mainly highlight central region in image classification, which is due to the fact that images for the classification task mainly contain object in the central region; whereas for scene images, it is hard for PerforatedCNN to focus on any specific location of the image. Note again that PerforatedCNN does not support either dynamic pixel routing or fully convolutional computation, requiring that the input image have a fixed size in order to learn fixed computation paths over the image. In contrast, our method is fully convolutional that is able to take as input images of arbitrary size and perform computing with input-dependent dynamic paths.

Table 9: Ablation study of the loss functions for surface normal estimation over NYUv2 dataset. Performance is measured by mean angular error (ang. err.) and the portion of prediction error within t° degree where $t = \{11.25, 22.50, 30.00\}$. Smaller ang. err. means better performance as marked by \downarrow .

metrics	cosine distance ($-\mathbf{n}^T \hat{\mathbf{n}}$)	inverse cosine ($\cos^{-1} \mathbf{n}^T \hat{\mathbf{n}}$)	cosine and inverse cosine
ang. err. \downarrow	23.3462	23.1191	22.7170
11.25 $^\circ$	0.3163	0.3279	0.3382
22.50 $^\circ$	0.5995	0.6093	0.6195
30.00 $^\circ$	0.7240	0.7302	0.7383

Table 10: Ablation study of at which layer to insert *MultiPool* module (with softmax weighted average, w-Avg.) for surface normal estimation on NYUv2 dataset. Performance is measured by mean angular error (ang. err.) and the portion of prediction error within t° degree where $t = \{11.25, 22.50, 30.00\}$. Smaller ang. err. means better performance as marked by \downarrow .

metrics	base.	MP@Res3	MP@Res4	MP@Res5	MP@Res6	MP@Res3-4	MP@Res3-5
ang. err. \downarrow	22.7170	21.9951	22.5506	21.9556	22.1661	22.5183	22.5051
11.25 $^\circ$	0.3382	0.3560	0.3366	0.3567	0.3514	0.3375	0.3389
22.50 $^\circ$	0.6195	0.6362	0.6188	0.6374	0.6323	0.6198	0.6209
30.00 $^\circ$	0.7383	0.7514	0.7386	0.7526	0.7482	0.7392	0.7394

Table 11: Comparison of MultiPool module with PAG and softmax weighted average (w-Avg.) over surface normal estimation on NYUv2 dataset. Performance is measured by mean angular error (ang. err.) and the portion of prediction error within t° degree where $t = \{11.25, 22.50, 30.00\}$. Smaller ang. err. means better performance as marked by \downarrow .

metrics	MP@Res3 (w-Avg.)	MP@Res3 (PAG)	MP@Res5 (w-Avg.)	MP@Res5 (PAG)
ang. err. \downarrow	21.9951	21.9793	21.9556	21.9226
11.25 $^\circ$	0.3560	0.3591	0.3567	0.3587
22.50 $^\circ$	0.6362	0.6396	0.6374	0.6384
30.00 $^\circ$	0.7514	0.7523	0.7526	0.7532

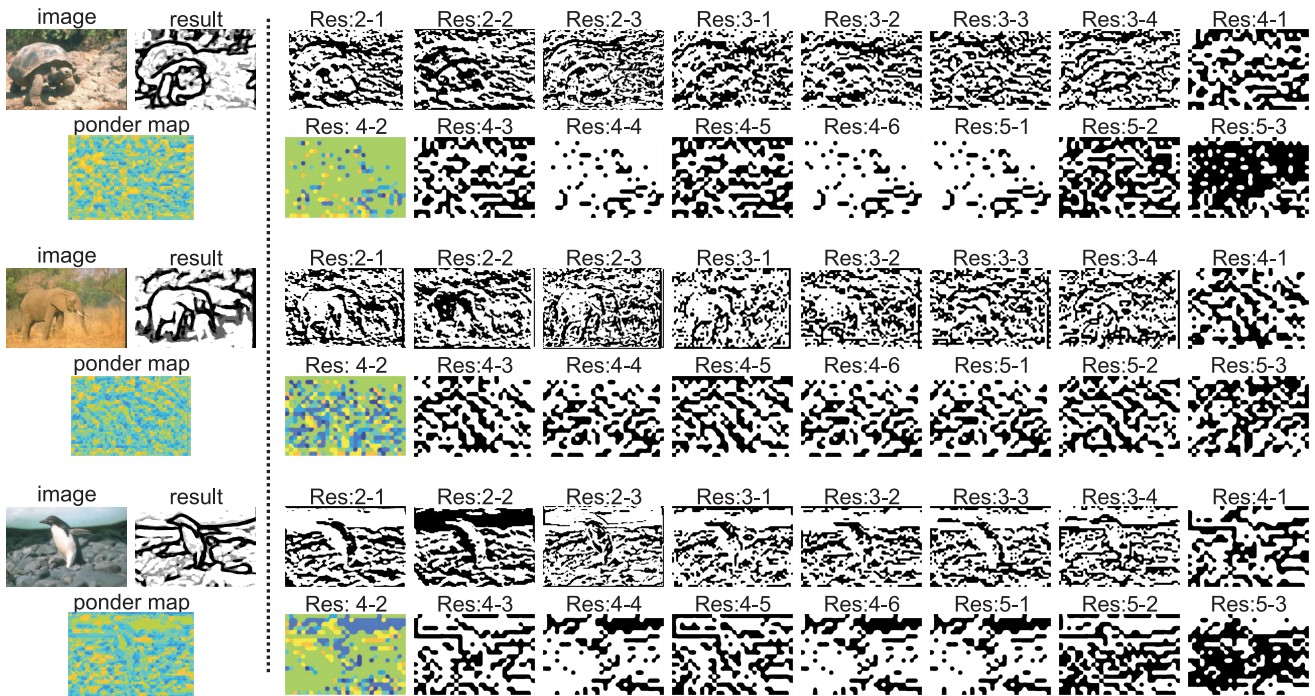


Figure 9: Visualization on BSDS500 dataset [1] of sparse binary attention maps at each layer for boundary detection, together with the output and ponder map accumulating all binary maps. PAG-based MultiPool module is inserted at layer Res4-2, which is not included in the ponder map.

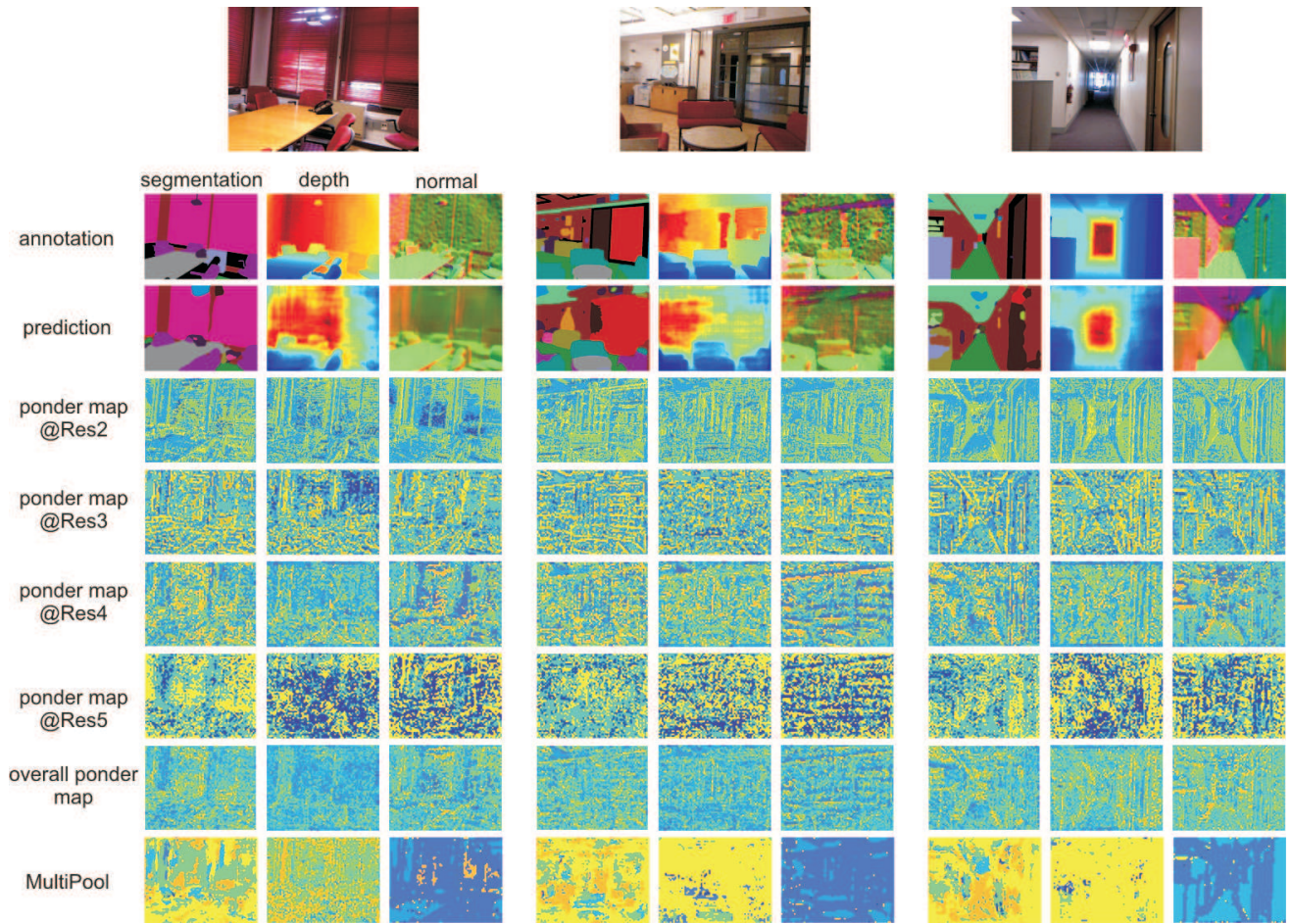


Figure 10: Visualization on NYUv2 dataset [12] for semantic segmentation, depth estimation and surface normal estimation. Besides the overall ponder map, we also show the partial ponder map for each macro residual block by summing the sparse binary attentional maps. The MultiPool binary masks are not included in the ponder maps.

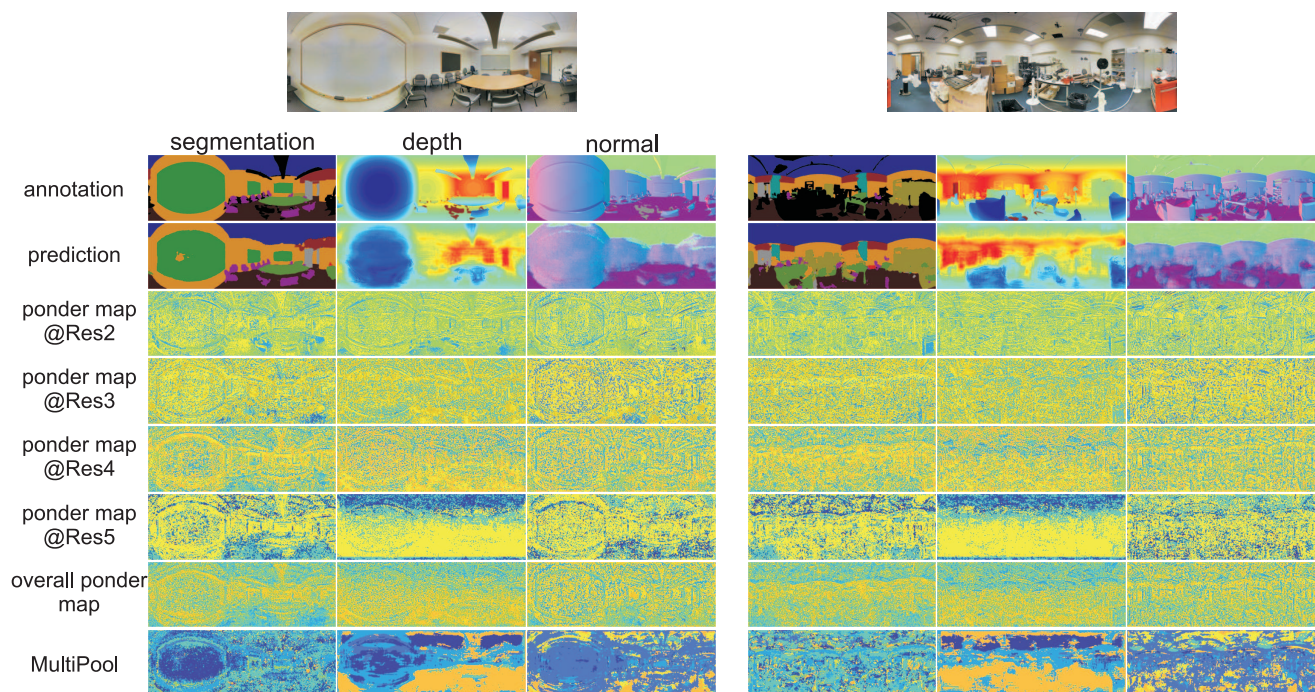


Figure 11: Visualization on Stanford2D3D [3] for semantic segmentation, depth estimation and surface normal estimation. Besides the overall ponder map, we also show the partial ponder map for each macro residual block by summing the sparse binary attentional maps. The MultiPool binary masks are not included in the ponder maps.

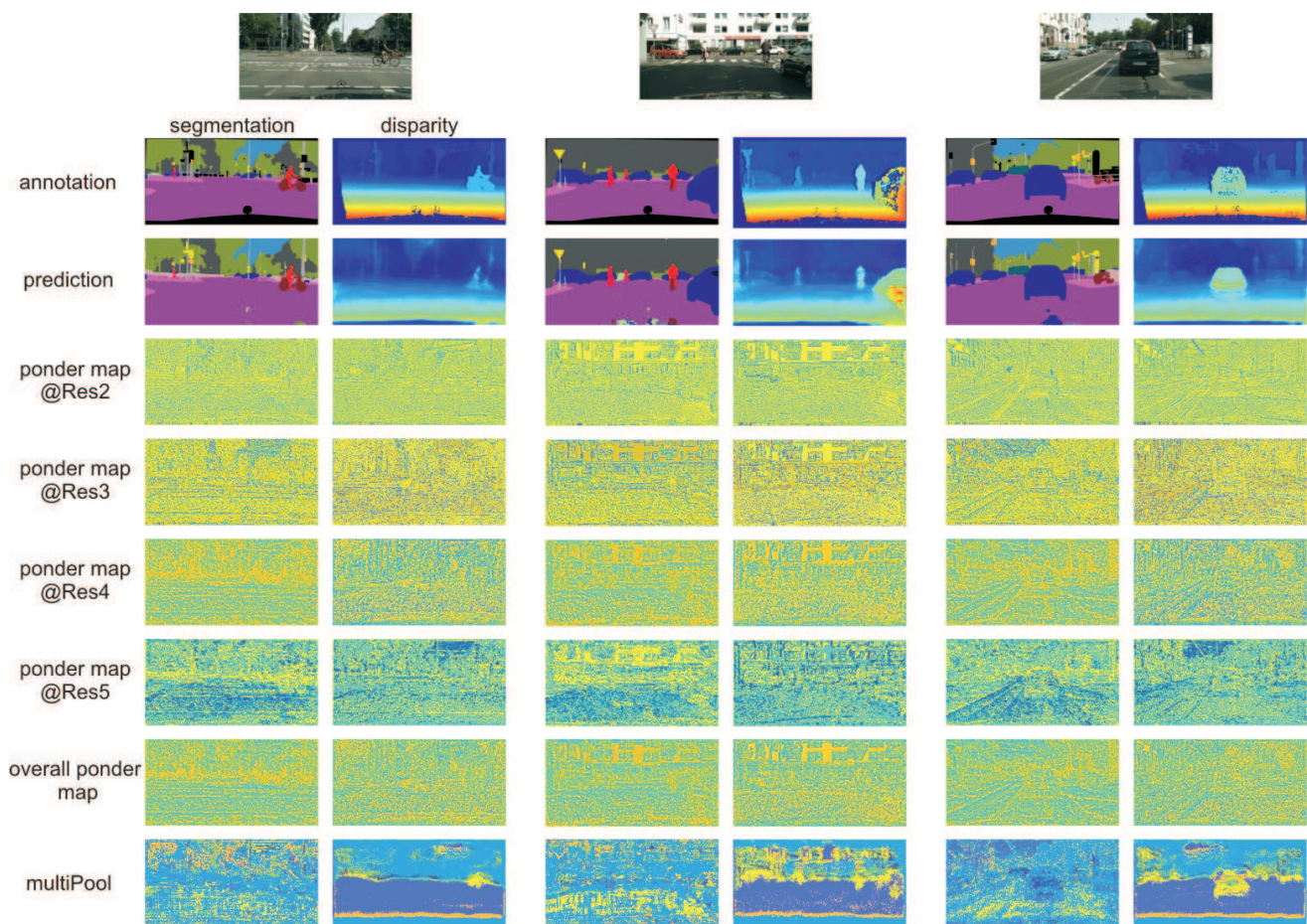


Figure 12: Visualization on Cityscapes dataset [10] for semantic segmentation and depth estimation. Besides the overall ponder map, we also show the partial ponder map for each macro residual block by summing the sparse binary attentional maps. The MultiPool binary masks are not included in the ponder maps.

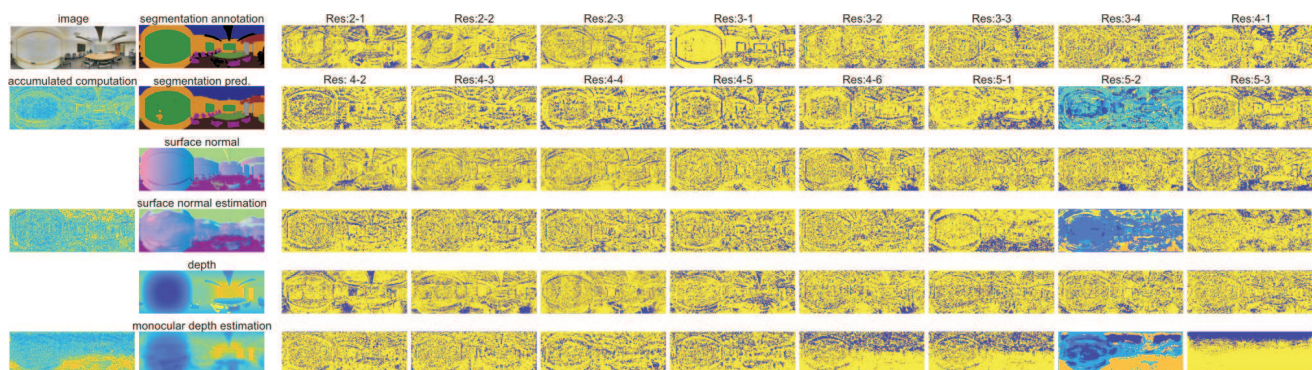


Figure 13: Visualization on Stanford2D3D [3] for semantic segmentation, surface normal estimation and depth estimation. Besides the overall ponder map (accumulated computation), we show all the binary maps produced by PAG, as well as the one in the MultiPool module at layer 5-2.

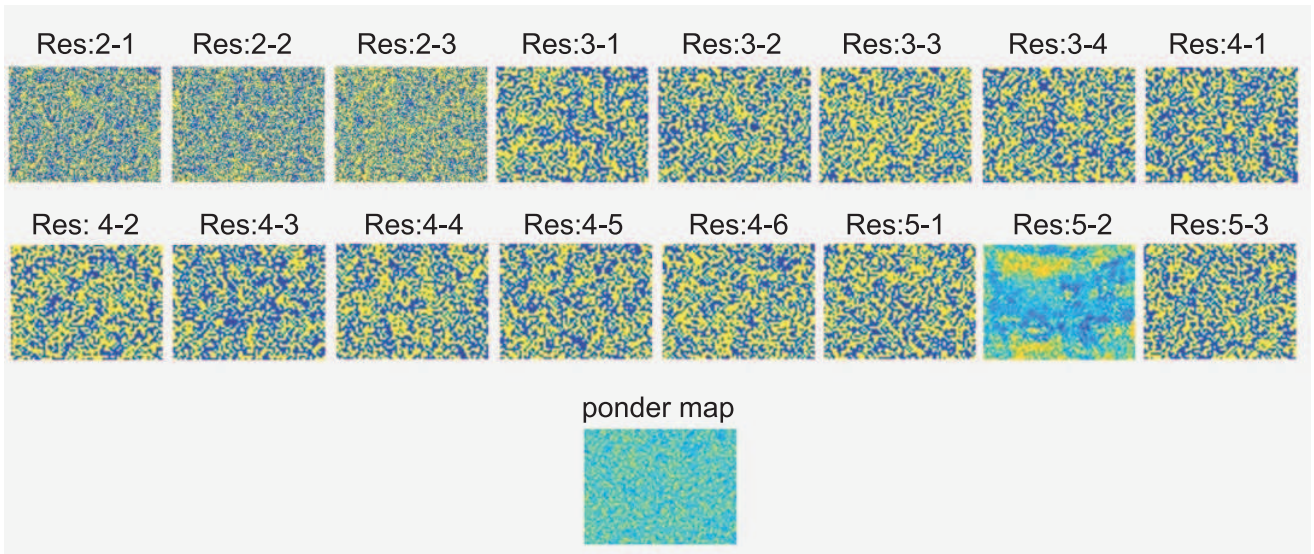


Figure 14: Visualization on binary masks trained by PerforatedCNN [16] on NYUv2 dataset for semantic segmentation. Note that we also insert a MultiPool module at Res5-2 block. This makes it fair to compare between our method and PerforatedCNN. We also accumulate all the binary masks towards the ponder map, from which we can see that the active pixels largely follow uniform distribution. This is different from what reported in [16] that the masks mainly highlight central region in image classification, which is due to the fact that images for the classification task mainly contain object in the central region; whereas for scene images, it is hard for PerforatedCNN to focus on any specific location of the image.